Design, Fabrication, and Characterization of a Helical Adaptive Multi-Material MicroRobot (HAMMR)

Liyuan Tan and David J. Cappelleri, *Member, IEEE*

Abstract—Adaptive locomotion is an advanced function of microrobots that can be achieved using smart materials. In this letter, a responsive hydrogel is utilized as a smart material and used to fabricate Helical Adaptive Multi-material MicroRobots (HAMMRs) with deformable tails to achieve adaptive locomotion capabilities. Moreover, a novel fabrication method is proposed to realize these types of helical microrobots with enhanced swimming performances by taking advantage of a strong magnetic head and deformable tail. The deformations of different tail designs and the fabricated microrobots are tested in different solvents. The swimming performances of the swimming microrobots are investigated experimentally under a rotating magnetic field and verified with theoretical calculations. The HAMMRs show significant deformations upon stimulation and changes in swimming performance which are in agreement with the scaled calculation result. Finally, the HAMMRs present an enhanced mobility with a highest published translational velocity for an adaptive swimming microrobot of 8.1 body length per second.

Index Terms—Micro/nano robots, soft robot materials and design, soft robot applications.

I. INTRODUCTION

MICROROBOTS, or microscale robots, have emerged in the last two decades. Microrobots have shown great potential in biomedical applications, such as biopsy [1], drug delivery [2], [3], and cell manipulation [4]. Swimming microrobots typically have flagella, similar to *Escherichia coli* bacteria and sperm, and use them to locomote through fluidic environments. The size and velocity of these organisms are so small that they swim at low Reynolds numbers, where viscous forces become dominant over the inertial forces [5], [6]. Investigations of these microorganisms have identified key features of their bodies for generating propulsion: their helical shapes and flexible nature.

As one of the main swimming strategies, numerous artificial helical-type microrobots have been fabricated in the last twenty years. Some typical fabrication methods of helical swimming microrobots are the self-scrolling method [7], two-photon polymerization (TPP) [8], [9], and glancing angle deposition [10]. However, these microrobots have bodies made from rigid materials so that the swimming performances are fixed once they are fabricated. Additional functionalities for these microrobots are typically achieved by an additional passive structure [9], [11] or by the motion of the microrobot utilizing the generated flow field [12], [13], [14].

However, more advanced functionalities are needed to achieve more complex behaviors, such as active micromanipulation, active drug delivery, and adaptive locomotion. The development of smart materials provides a way to realized the above functionalities. Smart materials are able to deform their shapes after fabrication and therefore introduce an additional degree-of-freedom when they are implemented into microrobots [15], [16]. Among those smart materials, hydrogels stand out because of their predominant biocompatibility, which is ideal for biomedical applications. Moreover, complex deformations have been demonstrated for hydrogels at the microscale via spacial designs of different stiffness with both mean and Gaussian curvatures. In the past few years, many hydrogels have been used to fabricate microrobots for different proposes, such as microgrippers for object manipulation [17], [18], [19], microcrawlers for locomotion [20], and helical microrobots for drug delivery [2] and directing cell chemotaxis [21].

Recently, hydrogels have been successfully studied and applied to microrobots for adaptive locomotion capabilities [22]. Huang et al. developed a photolithographic method to fabricate a helical-type microrobot with adaptive locomotion capabilities in environments with different viscosities, solute concentrations, and temperatures [23], [24]. Furthermore, the properties of the proposed hydrogel-based swimming microrobots have been well explored [25], [26]. Lee et al. demonstrated a hydrogel microroller passing through a narrow gap by actively increasing the environmental temperature to downsize the microroller [27].

Currently, photolithography and TPP are the two methods mainly adopted for fabricating hydrogel-based helical microrobots. Photolithography-based methods can only achieve helical ribbon structures with multi-layers or gradient structures due to the intrinsic 2D patterning scheme. These ribbon-like helical microrobots are not likely to perform well and/or have special requirements to make them swim with rotating magnetic fields. This is because a random distribution of magnetic nanoparticles in the structure will result in an overall magnetic moment that tends to align along the helical axis. Responsive
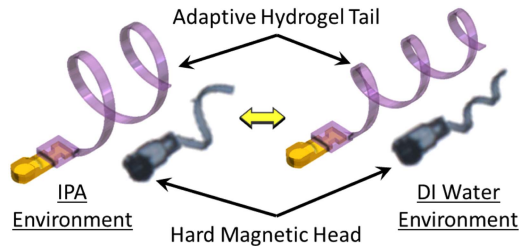
Fig. 1. Schematic of the Helical Adaptive Multi-material MicroRobot (HAMMR). It consists of a hard magnetic head and an adaptive helical hydrogel structures that deforms between a loose and compact configuration depending on the solvent environment. The HAMMR locomotion is controlled with a rotating magnetic field.

hydrogels printed via TPP suffer from a low concentration of the doped magnetic nanoparticles which results in a limited step-out frequency of the microrobot [27]. Recently, a surface-coating method has been proposed to increase the amount of magnetic nanoparticles incorporated in the TPP structures to overcome this low concentration issue [28]. However, even though some ribbon-like helical structures were printed and successfully coated, the swimming performance under a rotating magnetic field is not reported, most likely due to the lack of efficient magnetic moment caused by the randomly distributed nanoparticles.

In this letter, the design, fabrication, and testing of a novel Helical Adaptive Multi-material MicroRobot (HAMMR) are presented (Fig. 1). The proposed fabrication method allows for enhanced mobility through the combination of a deformable tail and a strong magnetic head. The fabrication method utilizes both photolithography and TPP techniques and uses multiple materials to construct the swimming microrobots. The fabricated microrobot has a head with strong magnetic materials while the helical tail is printed using a responsive hydrogel. The design of the tail has been analyzed for different geometric parameters and deformation capabilities in various solvent environments. Moreover, different design parameters have been selected for the fabricated microrobots for adaptive locomotion achieving different behaviors in different environments. The swimming performances of the swimming microrobot are studied experimentally and compared with theoretical calculations.

II. DESIGN & MODELING

A. Design Overview

Fig. 1 shows the schematic of a HAMMR while Fig. 2(a) shows details of the design parameters for the HAMMRs adaptive helical tail. The helical structures are modulated with soft and hard hydrogel regions while the soft regions are responsive to different solvents resulting in a deformation of the entire structure. In this letter, the helical structure undergoes a bidirectional deformation from a loose helix to a compact one after being transferred from IPA to DI water (Fig. 2(b) and (c)). This deformation is defined by the geometric parameters listed in Table I and the choice of modulating angle, θ. In both IPA and DI water, the soft regions of the structures
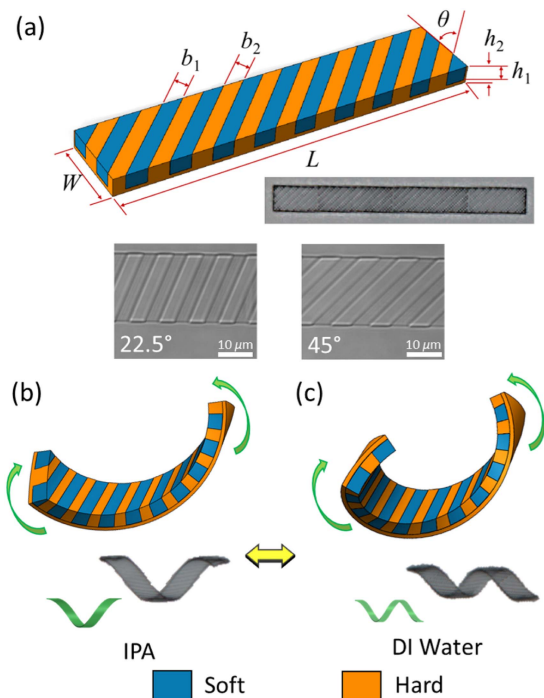

Fig. 2. Schematic of the HAMMR adaptive tail. Design parameters (a) and responses in different solvents (b) and (c).

TABLE I
DESIGN PARAMETERS

Parameter	Symbol	Value
Width	W	20 μm
Length	L	400 μm
Width of the soft region	b_1	4 μm
Width of the hard region	b_2	4 μm
Thickness of the modulating layer	h_1	4 μm
Total thickness	h_2	5 μm
Modulating angle	θ	0° to 90°

are deswelled comparing with the initial design while in DI water the deswelling is more significant (Fig. 2(c)). Due to the mismatch in stiffness and the size change, the printed planar strip is bent into different shapes depending on the modulating angle. The adaptive helical tail is combined with a hard magnetic head to create the HAMMR that can be controlled with a rotating magnetic field. Thus, once the geometry of the adaptive tail is known, we can model the dynamics of the helical swimming microrobot to evaluate its performance in different environments.

B. Modeling Microrobot Dynamics

The dynamics of a microrobot can be characterized by the force and torque balances [29], [30],

$$\begin{pmatrix} U \\ \Omega \end{pmatrix} = \begin{pmatrix} \mathcal{E} & \mathcal{G} \\ \mathcal{G}^T & \mathcal{F} \end{pmatrix} \begin{pmatrix} F \\ L \end{pmatrix}, \qquad (1)$$

where U and Ω are the translational and angular velocities of the microrobot, $\mathcal{G}$, $\mathcal{F}$, and $\mathcal{E}$ are the coupling, rotational, and translational mobility tensors of the microrobot, respectively,

that only depend on the geometry of the microrobot, and F and L are the forces and torques exerted on the microrobot.

For a swimming microrobot actuated by a uniform rotating magnetic field, (1) can be reduced to the following equations because F will be zero without a magnetic gradient [30], [31], [32].

$$U = \mathcal{G} \cdot L, \tag{2}$$

$$\Omega = \mathcal{F} \cdot L, \tag{3}$$

with $L = m \times H$ where m is normally defined with a body coordinate system (BCS) affixed to the magnetic microrobot while H is with a laboratory coordinate system (HCS) as an input parameter for actuation with a angular velocity of ω. However, these two coordinates can be related by a rotation matrix $\mathbf{R}$ so that $H^{BCS} = \mathbf{R} \cdot H^{HCS}$. The mobility tensors can be obtained by the multipole expansion method, which has been widely used for microrobots with arbitrary shapes, by discretizing the structure of the microrobot into spheres [33], [34]. Solving (3) in the in-sync regime where $\Omega = \omega$ gives the torque L for (2). Therefore,

$$U = \mathbf{R}^T \cdot \mathcal{G} \cdot \mathcal{F}^{-1} \cdot \Omega^{BCS}. \tag{4}$$

Finally, the translational velocity can be obtained by applying the dot product of the translational and the angular velocities, which is

$$U_Z \cdot \omega \cdot l = \Omega^{BCS} \cdot \mathcal{G} \cdot \mathcal{F}^{-1} \cdot \Omega^{BCS}, \tag{5}$$

where l is the characteristic dimension of the microrobot. Therefore, we can use (5) to determine the translational velocity of the HAMMRs in different geometric states.

III. HAMMR FABRICATION

The fabrication process of the microrobot is depicted in Fig. 3. It consists of three stages: 1) Photolithography; 2) TPP; and 3) Release. A 60 μm diameter magnetic disc is first patterned with a thin SU-8 adhesive layer followed by an SU-8/magnetic microparticle (MMP) mixture layer via photolithography on a coverslip (Fig. 3(i) and (ii)). The mixture contains SU-8 2025 with neodymium magnetic microparticles (MQFP-B, average diameter of 5 μm, Magnequench). It is achieved by mixing the particles into SU-8 with a weight ratio of 1 using a high-speed mixer. Next, a second layer of pure SU-8 is photolithographed with a pattern covering the magnetic disc and having an extruded fish-bone structure (Fig. 3(iii)). The fish-bone structure is designed to create a solid connection between the magnetic head and the helical responsive tail. After fabricating the fish-bone structure, the patterned coverslip is cut and transferred to a Physical Properties Measurement System (PPMS, Dynacool, Quantum Design) to magnetize the magnetic particles with a uniform 3 T magnetic field. Then, the magnetized sample is transferred to a commercial TPP system (Photonic Profession GT2, Nanoscribe GmbH) to have the connector (Fig. 3(iv)) and helical tail (Fig. 3(v)) printed. The connector also has a fish-bone design for enhancing the physical connection between the tail and magnetic head. The responsive helical tail is achieved by a responsive PNIPAM hydrogel polymerized with a 63x oil-immersion objective. Then the
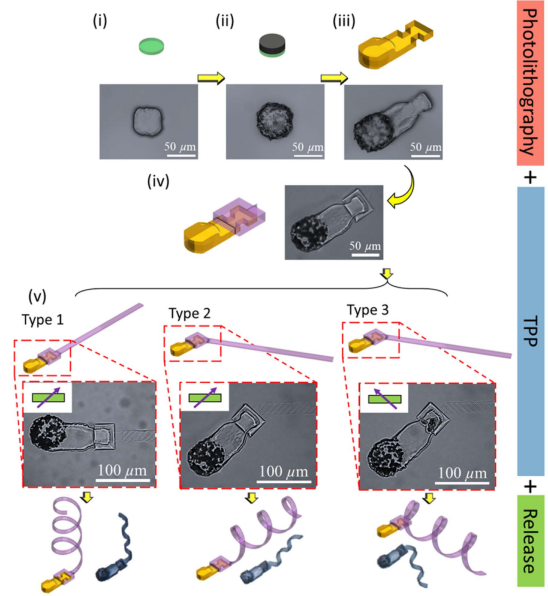

Fig. 3. Fabrication process and different types of HAMMRs. (i) Circular pure SU-8 adhesive layer. (ii) Circular magnetic disc with SU-8/MMPs. (iii) Pure SU-8 cover layer with a fish-bone design. (iv) Printing of the hydrogel connector. (v) Printing of the modulated helical hydrogel tails. Illustrations of three general types of head-tail designs and their corresponding resulting HAMMRs.

obtained microswimmers are developed in IPA for an hour and then immersed in DI water. The printed HAMMRs stay attached (non-released) to the substrate and can be released by tweezers.

The chemical-responsive poly-NIPAM (PNIPAM) hydrogel precursor is prepared following the process described in [35]. In brief, 1.6 g of N-isopropylacrylamide (NIPAM), 0.8 mL of acrylic acid (AAc), and 0.15 g polyvinylpyrrolidone (PVP) are dissolved in 1 mL of ethyl lactate (EL) followed by vigorous stirring for complete dissolution. Then 2.5 mL of the solution obtained above is mixed with 0.4 mL of dipentaerythritol pentaacrylate (DPEPA), 0.5 mL of triethanolamine (TEA), and 100 μL of 4,4'-bis(diethylamino)benzophenone/N,N-dimethylformamide (EMK/DMF) solution (1 to 4 weight ratio). The solution is magnetically stirred overnight to ensure complete dissolution.

The deformable helical tail is achieved by the printing of a planar structure with modulation of responsive and non-responsive strips. The soft regions are printed with a laser power (LP) of 15 mW and a scanning speed (SS) of 8 mm/s. The hard regions adopt an interpenetrating network and are initially printed with an LP of 30 mW and a SS of 8 mm/s. However, to ensure a solid connection between the soft and hard regions, the hard regions are also polymerized for a second time with the printing parameters of the soft regions. The summary of the design parameters can be found in Table I. In this letter, only the modulating angle is investigated for the demonstrations of the proposed swimming microrobot. The swelling performance of the soft and hard regions printed by those parameters can be found in [36].

Based on the orientation of the printed modulated strip with the magnetic head and the orientation of the modulating angle,
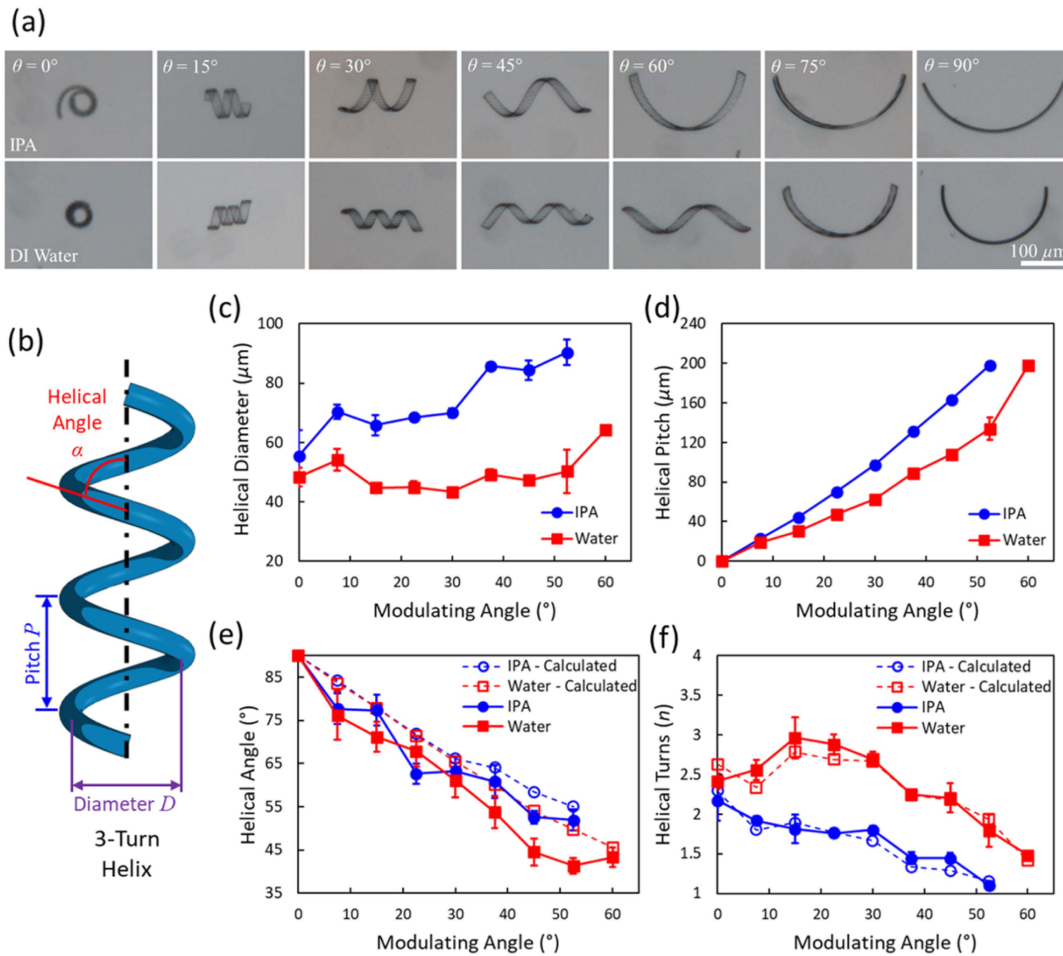
Fig. 4. Effects of modulating angle on the helical geometries. (a) Images of the resulting helical structures with different modulating angles. (b) Illustration of the parameters characterizing a helix. (c) Change of helical diameters (D) with modulating angles. (d) Change of helical pitches (P) with modulating angles. (e) Change of helical angles (α) with modulating angles. (f) Change of helical turns (n) with modulating angles. Dash lines in (e) and (f) are calculated values based on the measured diameters and pitches in (c) and (d).

there are generally three types of HAMMRs produced, as shown in Fig. 3(v). Type 1 HAMMRs have an initial tail printed in line with the magnetic head resulting in a HAMMR with a helical tail axis largely deviated from the head axis. The angle between the helical axis and the magnetic head depends on the modulating angle of the tail. Types 2 and 3 HAMMRs have their initial tail printed with an angle to the magnetic head. The difference between these two types is the orientation of the modulating angle. If the modulating direction is along the magnetic head, the resulting HAMMRs are likely to be a straight structure, with the helical axis coinciding with the axis of the magnetic head (Type 2). Other modulating angles that are not aligned with the magnetic head will lead to the Type 3 HAMMRs, which are similar to the Type 1 design.

IV. RESULTS AND DISCUSSION

A. Deformation of the Tail Geometry

The deformation of the tail design has been investigated with different modulating angles (θ). As can be seen in Fig. 4(a), the modulating angle of the planar modulated strip shows a

significant influence on the resulting geometrical shape of the helical structures. By printing the planar strips with different modulating angles from $0°$ to $90°$ with an increment of $7.5°$, the resulting helical structures are found to have more than 1 turn in both IPA and DI water for θ values between $15°$ to $52.5°$. Since the responsive regions deswell more in water, the helical structures present a more compacted form than in IPA. Fig. 4(b) provides an illustration of the parameters characterizing a helical structure.

Fig. 4(c)–(f) show the four key geometrical parameters of the helical structures verse the modulating angles. The geometrical parameters are extracted from the images like those in Fig. 4(a). Therefore, only the data of a helical structure with more than one turn are utilized. The helical diameter (D) (Fig. 4(c)) shows a linearly increasing trend in both IPA and water while a smaller diameter can be found for water due to the stronger deswelling. The diameter data for $0°$ and $7.5°$ in water are generally higher than the diameters at $15°$ since the helical structures are in a contacted form at those instances, which restricted the further deformation. The diameter values in water are more stable until an obvious increase is found after $52.5°$. However, the helical

pitch (P) shows a significant increase for both IPA and water (Fig. 4(d)). Fig. 4(e) and (f) show the helical angle (α) and turns (n) values that are obtained from measurements (solid lines) and calculations (dashed lines). The calculations are obtained based on the measured data for helical diameter and pitch and the following equations:

$$\alpha = \arctan\left(\frac{\pi D}{P}\right), \tag{6}$$

$$n = \frac{L}{\sqrt{(\pi D)^2 + P^2}}, \tag{7}$$

with L assumed to be consistent with the original design without change because of the non-responsive outside layer. At small modulating angles ($\theta < 30°$), the helical angles are consistent in both IPA and water because the resulting structures are compacted. As the modulating angle increases, a deviation is found with the helical angle, larger for IPA than in water. Generally, the helical angle is expected to have a complementary relationship with the modulating angle, $\alpha = 90° - \theta$, when the structure is in a compact state. The relationship agrees with the measured data for water until 52.5°. After 52.5°, it trends upwards for a larger helical angle than in the IPA. However, the calculated values show a more consistent decreasing trend and the values are slightly higher than the measured values. The helical turns are significantly larger when the structures are transferred from IPA to water. For example, the turn number at 30° in water is 1.50 times the turn number in IPA. The overall turns are also decreasing with the increased modulating angle for a given length L. The calculated turns show a consistent agreement with the measured values for both IPA and water.

B. Frequency Response of the Swimming Microrobots

Fig. 5(a) shows the deformation of different types of the achieved microrobots. Here, the magnetic heads are attached to the substrate while the helical tails are able to deform in different environments. Two modulating angles are chosen for the microrobot: 22.5° and 45°. The modulating angle of 22.5° is selected because the helical tail with this angle will deform into a compact helix which gives a reduced mobility in water while having a decent mobility in IPA. The modulating angle of 45° is picked as it is the middle value between 0° and 90° and the resulting tail gives regular helical geometries, typically with a large enough pitch when comparing with the width of the helical ribbon, in both IPA and water.

The magnetic properties of the swimming microrobots are estimated by a bulk magnetic film prepared with the same material used to achieve the magnetic head of the microrobots. The magnetic film is spin-coated on a coverslip with a total volume of 1.716 mm^3. The magnetic head of the microrobots are measured to have an average volume of 4545 μm^3, with an average diameter of 62 μm and an average thickness of 15 μm (thickness measured with a P-10 Profiler, KLA-Tencor). The magnetization curve of the magnetic film is shown in Fig. 5(b) with an inset showing a remanence of 0.19 emu. Then the average magnetic moment of each microrobot is estimated to

be 5.14×10^{-6} emu based on the volume ratio of the bulk film to the microrobot.

Fig. 5(c) gives an example of the swimming motion at 1 Hz of a microrobot with the Type 2 design and a modulating angle of 22.5°. The frequency responses of some microrobots are presented in Fig. 5(d) and (e) in water and IPA. All experiments are performed under room temperature (20.8 °C). Microrobots with Type 2 designs are selected for testing because the rotational axis of the entire microrobot is close to the axis of the helical tail which results in a preferable swimming motion. The geometries of those microrobots released to the test environments are in agreement with those before release. The experiments are performed on a magnetic field generator (MFG-100i, MagnebotiX) with a preset field strength of 5 mT. Fig. 5(d) gives the translational velocities of microrobots with a tail modulating angle of 22.5°. As can be seen from the plot, both the translational velocities of the microrobots in IPA and water increase with the field frequency with a synchronous behavior. Since the magnetic moments of the fabricated microrobots are predefined with a direction nearly perpendicular to the helical axis of the tail, the precessing angle of the microrobot should be close to zero so that the translational velocity is going to increase linearly until step-out. However, the velocities seem to reach a plateau at 200 Hz. This is because of the decrease of field strength of the magnetic field generator at high frequency: from 5 mT at 0 Hz to around 2.9 mT at 200 Hz, resulting in a drop in the translational velocity. However, a step-out frequency is not observed until 200 Hz when the slope goes to zero. The velocity of the microrobots in IPA is higher than in water while IPA has a viscosity 2.4 times the viscosity of water. The fastest translational velocities observed are 2.26 mm/s in IPA and 1.02 mm/s in water which is 8.1 body length per second (bps) and 3.5 bps, respectively, with corresponding body lengths of 280.3 μm and 294.3 μm.

The velocity results of microrobots with a tail modulating angle of 45° are presented in Fig. 5(e). The velocity profiles of this microrobot are significantly different then the ones with a tail modulating angle of 22.5°. The microrobots in water do not meet the step-out frequency before 200 Hz and the velocity is still showing an upward trend at 200 Hz with a velocity of 3.03 mm/s or 7.6 bps with a body length of 400.0 μm. However, in IPA, the microrobots show a faster increase rate but a step-out frequency is observed at around 100 Hz (with a highest velocity of 2.64 mm/s or 6.7 bps with a body length of 392.4 μm). This, there are large error bars around that frequency because of the difference of deformation for different samples. When the frequency is higher than 120 Hz, the velocity of the microrobot in water is faster then in IPA since the microrobot in IPA has switched to the high-frequency asynchronous regime. The error bars for data in IPA are much smaller than those in water. The possible reason for this difference is that the geometries of each microrobot are slightly different. This is due to the processing of the SU-8 head, which may leave residue on the substrate resulting in a difference in the printed geometries. Moreover, the resulting tail geometries are less compact than in water so that the difference in the shapes in water is exaggerated for an identical tail length. The velocity results for the HAMMRs in water show
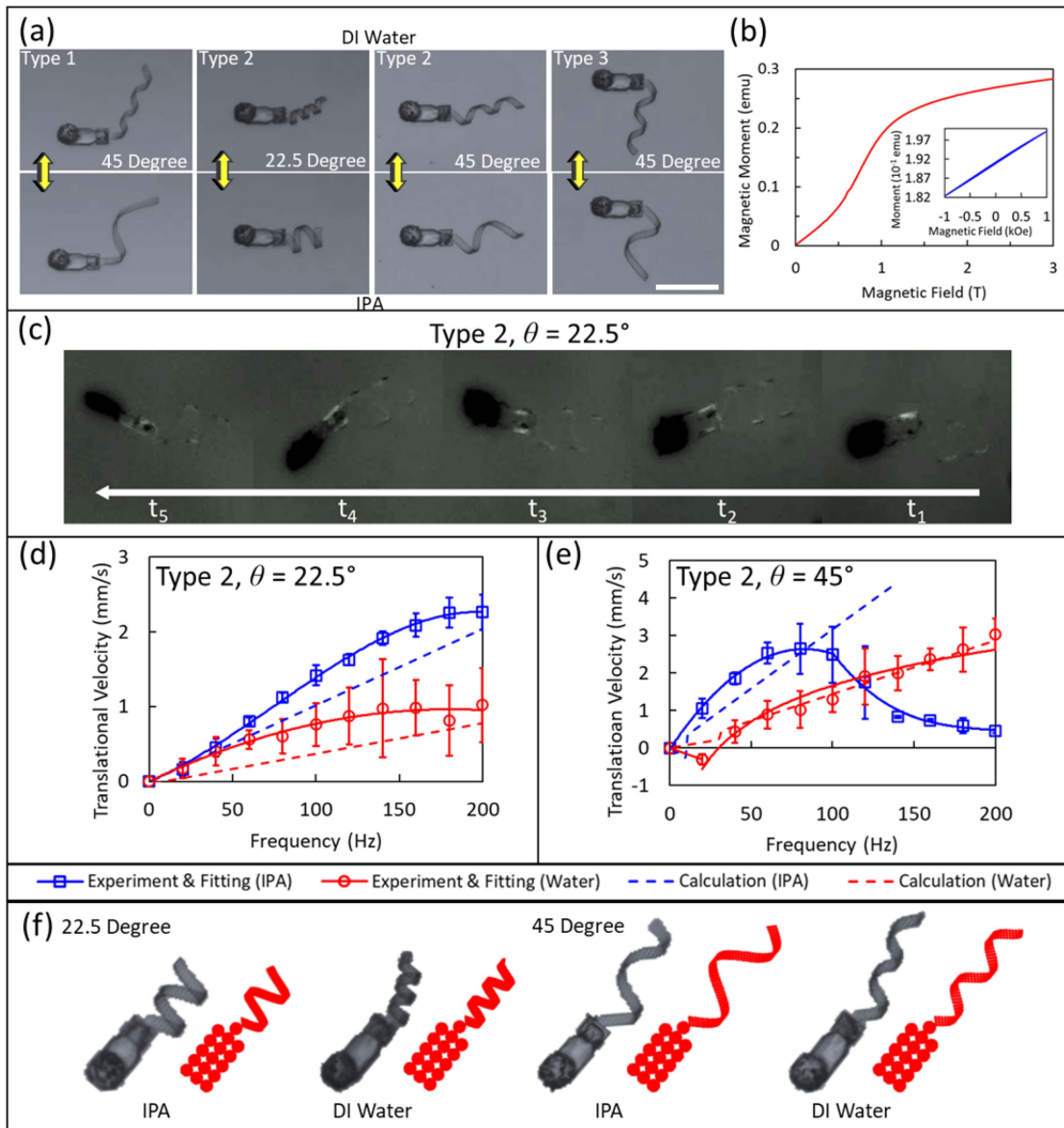
Fig. 5.   Responsive deformation and frequency responses of HAMMRs. (a) Deformation of different types and parameters of HAMMRs in DI water and IPA. Scale bar: 200 μm. (b) Magnetization and measurement of SU-8/MMPs film. (c) Swimming motion at 1 Hz of a Type 2 microrobot with a modulating angle of 22.5°. (d) Frequency response of a Type 2 HAMMR with a tail modulating angle of 22.5°. (e) Frequency response of a Type 2 HAMMR with a tail modulating angle of 45°. Curves and symbols in blue are data for HAMMRs in IPA while data in water are represented in red. Solid curves are fitted curves and dash lines are velocities predicted by the dynamics calculations. At least three microrobots are tested for each data point. (f) Discretizations of the microrobot geometries in (d) and (e) for the calculations using the multipole expansion method.

larger error bars most likely because the geometrical difference for each microrobot has been enlarged when they exhibit a more compact shape in water.

C. Theoretical Calculation of the Dynamics

Theoretical calculations of the dynamics of the microrobots before and after deformation have been performed based on the multipole expansion method. The discretization of the geometry of the microrobot is applied, separating the structure into spheres to calculate the mobility tensors. After solving the dynamics within the synchronous regime where $\Omega = \omega$, the

predicted velocity profiles for the microrobots can be achieved. The discretizations of the microrobots are provided in Fig. 5(f). The velocities are predicted with a total magnetic moment of 5×10^{-7} emu, a field strength of 2.9 mT (the field strength at 200 Hz), and viscosities of 1.0 mPa·s and 2.4 mPa·s for water and IPA, respectively. The direction of the magnetic moment is assumed to be perpendicular to the helical axis of the tail. The predicted velocities are shown in Fig. 5(d) and (e) with dash lines. As can be seen from the plots, the predicted velocities are generally in good agreement with experimental results. The discrepancy between the experimental results and the calculations is possibly because of the following reasons. First, the

TABLE II
APPROXIMATED HIGHEST REPORTED VELOCITIES OF ADAPTIVE OR 4D
PRINTED SWIMMING MICROROBOTS

Velocity (bps)	Year	Reference
0.7	2016	[23]
0.4	2018	[39]
5.3	2020	[40]
3.0	2020	[41]
2.7	2021	[42]
6.0	2021	[43]
1.8	2022	[44]
8.1	2022	This work

calculations are performed with a field strength of 2.9 mT while at the beginning of the experiments the field strength is closer to 5 mT for low operating frequencies. Second, the geometries of the microrobots are discretized with the helical axis of the tail in the same direction as the head axis, which is not exactly the case if they are slightly misaligned. Third, the magnetization direction of the magnetic head may not be perfectly perpendicular to the axis of the head in the actual fabricated microrobots. All the calculations show a continuously increasing trend up to 200 Hz except for the microrobot with a tail modulating angle of $45°$ in IPA. A step-out frequency is calculated at around 140 Hz as the red dash line ends in the figure, which is in agreement with the observed step-out frequency (around 100 Hz) from the experimental results. The calculation stops at 140 Hz predicting only the velocity in the synchronous regime since the velocity in the asynchronous regime is typically not adopted in applications. Comparing the two sample HAMMRs with different modulating angles, the one with a modulating angle of $45°$ achieved a higher translational velocity in both IPA and water. However, the magentic moment used to achieve all the calculations is 5×10^{-7} emu which is one-tenth of the experimental value of 5×10^{-6} emu. The possible reasons for this could be due to numerical problems solving the mobility tensors or some scaling effects for these kinds of helical geometries with a high aspect ratio, and rectangular cross-section, which restricts the largest radius that can be used to discretize the tails.

D. Enhanced Mobility by the Magnetic Head

It is of interest to implement microrobots with advanced functionalities. However, the importance of achieving microrobots with enhanced mobility cannot be ignored while considering the functionalities. Fast swimming microrobots can go upstream against the flow, which is especially important for bio-applications that require the microrobot to move within a blood vessel. However, torque-driven swimming microrobots fabricated via 3D or 4D printing typically have a low velocity. Additionally, it is difficult to incorporate magnetic materials into 4D printable materials [37], [38]. In this letter, the strong MMPs are used as the magnetic materials to achieve the magnetic microrobots achieving a high magnetic moment of 5.14×10^{-6} emu which results in the high translational velocity of 8.1 bps. Table II summaries and compares the highest velocities achieved by some adaptive or 4D printed swimming microrobots actuated by a rotating magnetic field. The table shows the enhanced mobility of the proposed HAMMRs while comparing with those recent works. Moreover, the HAMMRs can be incorporated with magnetic materials since the magnetic head can be achieved by multiple SU-8/MMPs layers and this will postpone the step-out frequency of the HAMMR and therefore increases the achievable velocity. Meanwhile, the initial field strength of the rotating magnetic field is 5 mT in this letter while it is normal to use a 10 to 20 mT field to actuate a swimming magnetic microrobot which is also helpful to achieve a higher velocity of the HAMMRs.

V. CONCLUSION

In this letter, we propose a novel fabrication method achieving helical swimming microrobots with multiple materials. The Helical Adaptive Multi-material MicroRobot, HAMMR, consists of a magnetic head prepared by SU-8 photoresist and MMPs, and a responsive hydrogel tail. The obtained swimming microrobots are able to perform adaptive locomotion, demonstrating various swimming performances under different environments. The deformations of tail designs with different modulating angles are investigated. Additionally, the deformations and swimming performances of the microrobots of different types caused by different orientations of tail and modulation are studied. Finally, the swimming performances have been verified by theoretical calculations based on the multipole expansion method.

The proposed novel fabrication method can be adaptive to various hydrogels with other responsiveness for different applications. For example, the hydrogel material used for the proposed swimming microrobot in this letter is also responsive to pH values which means this microrobot can also be used for biomedical application involving pH changes [35], [45]. The materials adopted for the head of the microrobots have shown promising biocompatiblities, which are also promising for bioapplications [46]. Other hydrogels that are thermal or light responsive can be applied to this method to realize HAMMRs that are adaptive under environmental or local temperature changes.

REFERENCES

[1] Q. Jin, Y. Yang, J. A. Jackson, C. Yoon, and D. H. Gracias, "Untethered single cell grippers for active biopsy," *Nano Lett.*, vol. 20, no. 7, pp. 5383–5390, 2020.

[2] H. Lee, D. I. Kim, S. H. Kwon, and S. Park, "Magnetically actuated drug delivery helical microrobot with magnetic nanoparticle retrieval ability," *ACS Appl. Mater. Interfaces*, vol. 13, no. 17, pp. 19633–19647, 2021.

[3] D. Gong, N. Celi, D. Zhang, and J. Cai, "Magnetic biohybrid microrobot multimers based on chlorella cells for enhanced targeted drug delivery," *ACS Appl. Mater. Interfaces*, vol. 14, no. 5, pp. 6320–6330, 2022.

[4] W. Chen, H. Zhou, B. Zhang, Q. Cao, B. Wang, and X. Ma, "Recent progress of micro/nanorobots for cell delivery and manipulation," *Adv. Funct. Mater.*, vol. 2110625, pp. 1–15, 2022.

[5] E. M. Purcell, "Life at low Reynolds number," *Amer. J. Phys.*, vol. 45, no. 1, pp. 3–11, 1977.

[6] L. Tan, J. Ali, U. Cheang, X. Shi, D. Kim, and M. Kim, "μ-PIV measurements of flows generated by photolithography-fabricated achiral microswimmers," *Micromachines*, vol. 10, no. 12, 2019, Art. no. 865.

[7] L. Zhang, J. J. Abbott, L. Dong, B. E. Kratochvil, D. Bell, and B. J. Nelson, "Artificial bacterial flagella: Fabrication and magnetic control," *Appl. Phys. Lett.*, vol. 94, no. 6, 2009, Art. no. 064107.

[8] M. Suter et al., "Superparamagnetic microrobots: Fabrication by two-photon polymerization and biocompatibility," *Biomed. Microdevices*, vol. 15, no. 6, pp. 997–1003, 2013.

[9] S. Tottori, L. Zhang, F. Qiu, K. K. Krawczyk, A. Franco-Obregõn, and B. J. Nelson, "Magnetic helical micromachines: Fabrication, controlled swimming, and cargo transport," *Adv. Mater.*, vol. 24, no. 6, pp. 811–816, 2012.

[10] D. Schamel et al., "Nanopropellers and their actuation in complex viscoelastic media," *ACS Nano*, vol. 8, no. 9, pp. 8794–8801, 2014.

[11] T. Y. Huang et al., "3D printed microtransporters: Compound micromachines for spatiotemporally controlled delivery of therapeutic agents," *Adv. Mater.*, vol. 27, no. 42, pp. 6644–6650, 2015.

[12] Z. Ye and M. Sitti, "Dynamic trapping and two-dimensional transport of swimming microorganisms using a rotating magnetic microrobot," *Lab Chip*, vol. 14, no. 13, pp. 2177–2182, 2014.

[13] Q. Zhou, T. Petit, H. Choi, B. J. Nelson, and L. Zhang, "Dumbbell fluidic tweezers for dynamical trapping and selective transport of microobjects," *Adv. Funct. Mater.*, vol. 27, no. 1, 2017, Art. no. 1604571.

[14] X. Fan et al., "Automated noncontact micromanipulation using magnetic swimming microrobots," *IEEE Trans. Nanotechnol.*, vol. 17, no. 4, pp. 666–669, Jul. 2018.

[15] L. Tan, A. C. Davis, and D. J. Cappelleri, "Smart polymers for microscale machines," *Adv. Funct. Mater.*, vol. 31, no. 9, pp. 1–56, 2021.

[16] G. Adam, A. Benouhiba, K. Rabenorosoa, C. Clévy, and D. J. Cappelleri, "4D printing: Enabling technology for microrobotics applications," *Adv. Intell. Syst.*, vol. 3, no. 5, 2021, Art. no. 2000216.

[17] J. C. Breger et al., "Self-folding thermo-magnetically responsive soft microgrippers," *ACS Appl. Mater. Interfaces*, vol. 7, no. 5, pp. 3398–3405, 2015.

[18] F. Ongaro et al., "Control of untethered soft grippers for pick-and-place tasks," in *Proc. IEEE RAS EMBS Int. Conf. Biomed. Robot. Biomechatron.*, 2016, pp. 299–304.

[19] H. Jia et al., "Universal soft robotic microgripper," *Small*, vol. 15, no. 4, pp. 1–8, 2019.

[20] I. Rehor et al., "Photoresponsive hydrogel microcrawlers exploit friction hysteresis to crawl by reciprocal actuation," *Soft Robot.*, vol. 8, no. 1, pp. 10–18, 2021.

[21] Z. Wang et al., "Magnetic helical hydrogel motor for directing T cell chemotaxis," *Adv. Funct. Mater.*, vol. 31, no. 25, pp. 1–8, 2021.

[22] L. Tan and D. J. Cappelleri, "Modeling of bilayer hydrogel springs for microrobots with adaptive locomotion," in *Proc. IEEE/RSJ Int. Conf. Intell. Robots Syst.*, 2021, pp. 8530–8537.

[23] H. W. Huang, M. S. Sakar, A. J. Petruska, S. Pané, and B. J. Nelson, "Soft micromachines with programmable motility and morphology," *Nature Commun.*, vol. 7, pp. 1–10, 2016.

[24] H. W. Huang, F. E. Uslu, P. Katsamba, E. Lauga, M. S. Sakar, and B. J. Nelson, "Adaptive locomotion of artificial microswimmers," *Sci. Adv.*, vol. 5, no. 1, pp. 1–8, 2019.

[25] H. W. Huang, Q. Chao, M. S. Sakar, and B. J. Nelson, "Optimization of tail geometry for the propulsion of soft microrobots," *IEEE Robot. Automat. Lett.*, vol. 2, no. 2, pp. 727–732, Apr. 2017.

[26] H. W. Huang et al., "Investigation of magnetotaxis of reconfigurable micro-origami swimmers with competitive and cooperative anisotropy," *Adv. Funct. Mater.*, vol. 28, 2018, Art. no. 1802110.

[27] Y. W. Lee, H. Ceylan, I. C. Yasa, U. Kilic, and M. Sitti, "3D-Printed multi-stimuli-responsive mobile micromachines," *ACS Appl. Mater. Interfaces*, vol. 13, no. 11, pp. 12759–12766, 2021.

[28] S. Ji, X. Li, Q. Chen, P. Lv, and H. Duan, "Enhanced locomotion of shape morphing microrobots by surface coating," *Adv. Intell. Syst.*, vol. 3, no. 7, 2021, Art. no. 2000270.

[29] J. Happel and H. Brenner, *Low Reynolds Number Hydrodynamics - With Special Applications to Particulate Media*, vol. 1. Berlin, Germany:Springer, 1983.

[30] K. I. Morozov, Y. Mirzae, O. Kenneth, and A. M. Leshansky, "Dynamics of arbitrary shaped propellers driven by a rotating magnetic field," *Phys. Rev. Fluids*, vol. 2, no. 4, pp. 1–29, 2017.

[31] Y. Mirzae, O. Dubrovski, O. Kenneth, K. I. Morozov, and A. M. Leshansky, "Geometric constraints and optimization in externally driven propulsion," *Sci. Robot.*, vol. 3, no. 17, 2018, Art. no. eaas8713.

[32] J. Sachs et al., "Role of symmetry in driven propulsion at low Reynolds number," *Phys. Rev. E*, vol. 98, no. 6, pp. 1–12, 2018.

[33] A. V. Filippov, "Drag and torque on clusters of N arbitrary spheres at low Reynolds number," *J. Colloid Interface Sci.*, vol. 229, no. 1, pp. 184–195, 2000.

[34] R. S. Berman, O. Kenneth, J. Sznitman, and A. M. Leshansky, "Undulatory locomotion of finite filaments: Lessons from caenorhabditis elegans," *New J. Phys.*, vol. 15, 2013, Art. no. 075022.

[35] D. Jin, Q. Chen, T. Y. Huang, J. Huang, L. Zhang, and H. Duan, "Four-dimensional direct laser writing of reconfigurable compound micromachines," *Mater. Today*, vol. 32, pp. 19–25, 2020. [Online]. Available: https://doi.org/10.1016/j.mattod.2019.06.002

[36] L. Tan, H. Lee, L. Fang, and D. J. Cappelleri, "A power compensation strategy for achieving homogeneous hydrogels : Out-of-plane variations," *Gels*, vol. 8, no. 12, 2022, Art. no. 828.

[37] F. Rajabasadi, L. Schwarz, M. Medina-Sánchez, and O. G. Schmidt, "3D and 4D lithography of untethered microrobots," *Prog. Mater. Sci.*, vol. 120, 2021, Art. no. 100808.

[38] M. Medina-Sánchez, V. Magdanz, M. Guix, V. M. Fomin, and O. G. Schmidt, "Swimming microrobots: Soft, reconfigurable, and smart," *Adv. Funct. Mater.*, vol. 28, no. 25, pp. 1–27, 2018.

[39] X. Wang et al., "3D printed enzymatically biodegradable soft helical microswimmers," *Adv. Funct. Mater.*, vol. 28, no. 45, pp. 1–8, 2018.

[40] J. Giltinan, V. Sridhar, U. Bozuyuk, D. Sheehan, and M. Sitti, "3D Microprinting of iron platinum nanoparticle-based magnetic mobile microrobots," *Adv. Intell. Syst.*, vol. 3, no. 1, 2021, Art. no. 2000204.

[41] I. C. Yasa, H. Ceylan, U. Bozuyuk, A.-M. Wild, and M. Sitti, "Elucidating the interaction dynamics between microswimmer body and immune system for medical microrobots," *Sci. Robot.*, vol. 5, no. 43, 2020, Art. no. eaaz3867.

[42] J. Liu et al., "Magnetically propelled soft microrobot navigating through constricted microchannels," *Appl. Mater. Today*, vol. 25, 2021, Art. no. 101237. [Online]. Available: https://doi.org/10.1016/j.apmt.2021.101237

[43] F. Zhao, W. Rong, L. Wang, and L. Sun, "Magnetic actuated shape-memory helical microswimmers with programmable recovery behaviors," *J. Bionic Eng.*, vol. 18, no. 4, pp. 799–811, 2021.

[44] H. Zhang et al., "Shape memory alloy helical microrobots with transformable capability towards vascular occlusion treatment," *Research*, vol. 2022, pp. 1–13, 2022.

[45] T. Huang et al., "Four-dimensional micro-building blocks," *Sci. Adv.*, vol. 6, no. 3, pp. 1–10, 2020.

[46] E. E. Niedert et al., "A tumbling magnetic microrobot system for biomedical applications," *Micromachines*, vol. 11, no. 9, 2020, Art. no. 861.